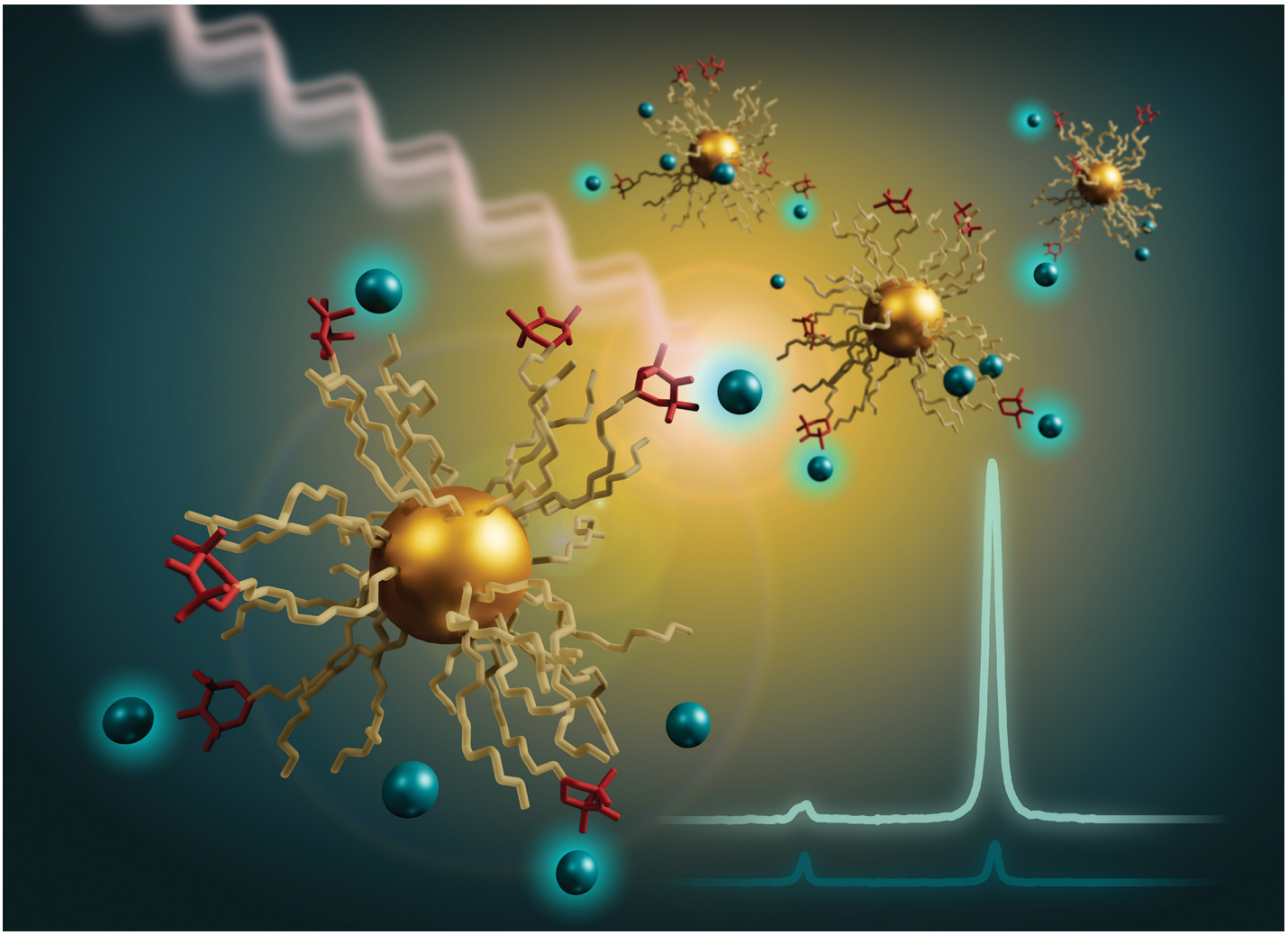

Showcasing collaborative research between the groups of Dr Tomas Orlando at the Natl. High Magnetic Field Laboratory, and Prof. Federico Rastrelli at the University of Padova.

Nanoparticle-assisted dynamic nuclear polarization in liquids

Gold nanoparticles coated with self-assembled monolayers (AuNPs) can serve as magnetization reservoirs in nuclear magnetic resonance experiments, making them attractive chemosensors. This study explored using electron–nucleus interactions for Overhauser effect dynamic nuclear polarization with AuNPs functionalized by radical- and recognition-bearing thiols. Experiments on chloroform/methanol mixtures showed significant chloroform enhancements but limited methanol response. Results demonstrate AuNPs' potential as polarizing agents, encouraging future design for selective hyperpolarization applications.

Image reproduced by permission of Tomas Orlando and Federico Rastrelli from *Phys. Chem. Chem. Phys.*, 2025, **27**, 22366. Cover Design: Tomas Orlando and Kevin John (NHMLF)

As featured in:

See Federico Rastrelli, Tomas Orlando *et al.*, *Phys. Chem. Chem. Phys.*, 2025, **27**, 22366.

ROYAL SOCIETY OF CHEMISTRY

rsc.li/pccp

Registered charity number: 207890

PCCP Owner Societies

PCCP

PAPER

View Article Online
View Journal | View Issue

Cite this: *Phys. Chem. Chem. Phys.*, 2025, **27**, 22366

Nanoparticle-assisted dynamic nuclear polarization in liquids

Beatrice Bernadette Mascitti, [a] Giordano Zanoni, [a] Alex van der Ham, [b] Luming Yang, [b] Lorenzo Franco, [a] Fabrizio Mancin, [a] Federico Rastrelli *[a] and Tomas Orlando *[c]

Gold nanoparticles (AuNPs) protected with self-assembled organic monolayers represent versatile nanostructures with applications in catalysis, molecular sensing, and recognition. The ordered arrangement of ligands within the monolayer promotes specific orientations and proximities of functional groups, facilitating weak yet selective interactions with small molecules in solution. In the context of nuclear magnetic resonance (NMR), AuNPs can act as magnetization reservoirs, allowing selective transfer to interacting molecules and making them promising chemosensors. While ''NMR chemosensing'' typically exploits nucleus–nucleus magnetization transfer mechanisms, we explored the potential of electron–nucleus interactions to allow selectively enhanced Overhauser effect dynamic nuclear polarization (OE-DNP). To this aim, we designed AuNPs simultaneously functionalized with two different thiols: a radical-bearing thiol as a polarizing agent for OE-DNP and an organic thiol tailored with different head groups to impart selective recognition. To evaluate both the polarization transfer efficiency and the selectivity, we performed OE-DNP experiments on a mixture of chloroform and methanol. Our results show sizeable enhancements on chloroform, possibly limited only by the mobility of the radical. On the other hand, the affinity for methanol does not correspond to greater enhancements on this target molecule. Although the system, as designed, does not provide efficient DNP on methanol as expected, our results confirm that AuNPs may be used as polarizing agents at magnetic fields up to 9.4 T. We foresee that future modifications of the nanoparticles' monolayer will allow the combination of spin polarization transfer efficiency with molecular recognition, offering a novel strategy to boost hyperpolarization techniques and expanding their application towards NMR detection of specific analytes.

Received 28th June 2025,
Accepted 12th August 2025

DOI: 10.1039/d5cp02465j

rsc.li/pccp

Introduction

Gold nanoparticles (AuNPs) protected by monolayers of organic molecules are self-organized and multivalent entities able to perform different functions.[1–3] Their applications in a variety of contexts have been extensively demonstrated and reviewed, spanning fields as diverse as bioimaging, nanomedicine, sensing and catalysis.[4–10]

The large interest in this class of molecular systems arises because the self-assembly of a monolayer of ligands onto the surface of a metal core offers a distinct pathway for achieving ordered and rather complex molecular architectures. Within the monolayer, in fact, the ligands are aligned and kept in close proximity, which restricts the possible configurations. These arrangements enable cooperative interactions that can be exploited to execute defined tasks such as, for example, molecular recognition.

The combination of NMR and AuNPs endowed with predefined binding affinity for specific classes of molecules lies at the basis of ''NMR chemosensing''.[11] In fact, the reduced rotational diffusion constants of NPs provide a magnetization reservoir within the monolayer that can be selectively transferred *via* nuclear Overhauser effect (NOE) only to molecules interacting with the monolayer. As such, when employed in the analysis of complex mixtures, NMR chemosensing typically provides an edited NMR spectrum showing only the signals of specific target molecules.

In recent years, NMR chemosensing has established remarkable achievements in terms of selectivity, and the advent of ''high-power'' water saturation transfer difference (STD) experiments allowed to partly overcome the inherent sensitivity

[a] *Department of Chemical Sciences, University of Padova, Padova, Italy. E-mail: federico.rastrelli@unipd.it*
[b] *ESR Spectroscopy Group, Max Planck Institute for Multidisciplinary Sciences, Göttingen, Germany*
[c] *National High Magnetic Field Laboratory and Florida State University, Tallahassee, FL, USA. E-mail: torlando@magnet.fsu.edu*

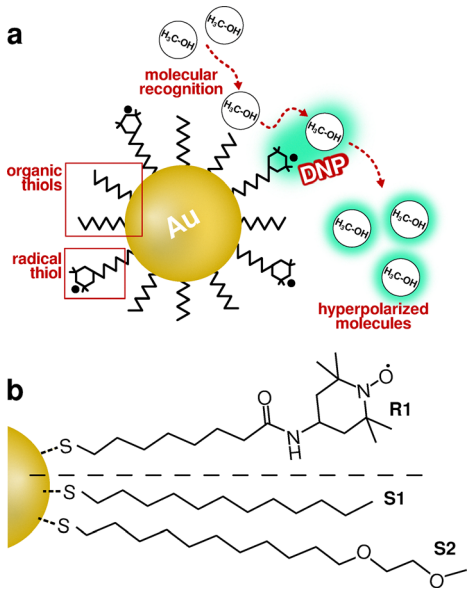

Fig. 1 (a) Cartoon of the DNP-chemosensing experiment. (b) Gold nanoparticles functionalized with the deprotected radical thiol **R1** and coated with organic thiols **S1** or **S2**.

limitations.[9,12] In this context, it seems plausible to investigate whether the nucleus–nucleus dipolar interactions at the basis of the chemosensing phenomenon can be paralleled by electron–nucleus interactions, which would open the pathway to hyperpolarized chemosensing experiments *via* electron–nuclear polarization transfer (Fig. 1a).

Among the various existing hyperpolarization techniques[13] – some of which successfully used for selective chemosensing,[14,15] dynamic nuclear polarization based on the Overhauser effect (OE-DNP) in the liquid state seems the most appropriate for our applications. In OE-DNP, high electron spin polarization is transferred to nearby nuclear spins *via* electron–nuclear cross-relaxation enabled by microwave irradiation, thereby enhancing their NMR signal.[16–19] The efficiency of OE-DNP at high magnetic fields depends on two factors:[20] (i) the presence of a large (a few MHz) electron–nuclear coupling,[20–23] often favoured by non-covalent interactions, such as hydrogen bonds,[24,25] halogen bonds,[26–28] or van der Waals interactions.[29] (ii) The presence of fast dynamics (enabled by molecular diffusion, collisions, structural reorientations, *etc.*)[22,30–33] that modulate the electron–nuclear couplings on the picoseconds or sub-picoseconds timescale.[34,35] In the context of ^{13}C-OE-DNP, those conditions are satisfied in systems constituted by an organic radical such as nitroxide as a polarizing agent (PA) and small molecules as OE-DNP targets. Although small molecules in low viscosity media perform significantly better than systems characterized by slower dynamics,[36–39] it has been recently proven that OE-DNP can be effective in viscous matrices like lipid bilayers,[40–42] and even on solid surfaces.[43] Similarly, bulky polarizing agents such as BDPA radical[29,44,45] or substrates functionalized with nitroxide[33,46–48] could be used as PAs in DNP, and their efficacy relies not only on OE-DNP but also on other mechanisms that work in liquids under specific circumstances.[40,41,49–51] In the same context, other groups have explored the idea of grafting a PA on solid beads to polarize *via* OE-DNP a flowing liquid,[46,47,52,53] or to use OE-DNP as a tool to explore the complex surface dynamics.[54–56]

With the aim of achieving DNP-enhanced chemosensing (Fig. 1a) and considering the requirements for efficient OE-DNP, we designed and synthesized gold nanoparticles (AuNPs) <2 nm in diameter functionalized with two surface ligands (Fig. 1b). The first ligand is a thiol (**R1**) featuring a nitroxide radical (one of the most efficient PAs for ^{13}C-DNP of small molecules in liquids) as a head group, and a C_7 aliphatic spacer (Fig. 1b), which provides enough molecular mobility to favour fast dynamics and limit the downsides arising from the large size of the AuNPs. The second ligand is a thiol that either acts as an inert "dilutant" (**S1**) or can form non-covalent interactions (namely hydrogen bonds) with suitable target molecules (**S2**) On the OE-DNP side, we selected two target molecules: chloroform, which gives high DNP enhancements at high magnetic field, and methanol, which is prone to interact with the oxomethylene groups of thiol **S2**. Their performance was compared to that of the free nitroxide radical TEMPOL and TEMPONE. Our results show that AuNPs can be used as PAs for OE-DNP at high magnetic fields (9.4 T). Although the molecular recognition properties do not offer a significant advantage to boost OE-DNP performance, AuNPs remain promising systems for OE-DNP, and their versatility in terms of chemical functionalization make these systems an optimal platform to achieve selective NMR hyperpolarization in liquids.

Materials and methods

Synthesis and functionalization of AuNPs

The AuNPs in this work were prepared following a two-step procedure involving the spontaneous formation of gold cores in solution through the reduction of gold salts (see SI). In general, a weak ligand (dioctylamine) is initially employed and then exchanged with a thiol: this procedure is known to improve the size control of the final nanoparticles.

The ligand TM-thiol **R1** carrying the TEMPO headgroup was synthesized with the procedure outlined in Scheme 1, involving the condensation of 8-(acetylthio)octanoic acid with 4-amino TEMPO. The insertion of TM-thiol **R1** in AuNPs covered with homogeneous monolayers of **S1** was realized by chemical exchange (see SI for details) to obtain nanoparticles **R1S1-AuNP**. Nanoparticles **R1S2-AuNP** were obtained from direct synthesis, meaning that both **R1** and **S2** were added in the desired proportions to form a mixed monolayer. Similar AuNPs functionalized with radicals have been prepared with a different protocol by Chechik *et al.*, 2004.[57]

Sample preparation for magnetic resonance spectroscopy

Solvents ($CHCl_3$, ^{13}C-methanol, methanol) and radicals (TEMPOL: 4-Hydroxy-TEMPO and TEMPONE: 4-Oxo-TEMPO) were

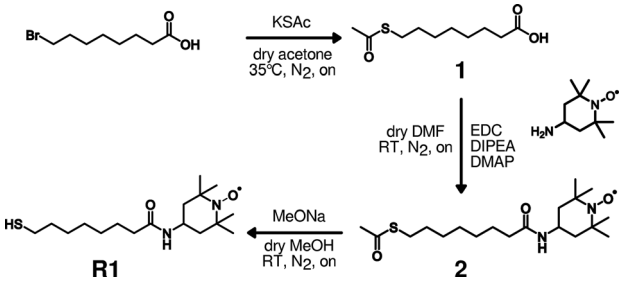

Scheme 1 Synthetic scheme of TM-thiol **2** which is then grafted on the particle as radical thiol **R1**.

used as received from the supplier, while ^{13}C-$CHCl_3$ was stabilized with 1% of ethanol and K_2CO_3 was added to neutralize acid species in solution. Samples for magnetic resonance measurements were prepared by dissolving the PA (nitroxide or **R1SX-AuNP**s) in the organic solvent used as target for DNP experiments. To reduce the content of dissolved oxygen, all samples were degassed with at least three freeze–pump–thaw cycles and then transferred in quartz tubes that were either flame-sealed or closed with air-tight caps.

Electron paramagnetic resonance (EPR)

CW-EPR was used to probe whether the radical thiols are bound to the AuNPs, quantify their actual concentration, and evaluate their mobility compared to the unbound nitroxide radical.

Electron paramagnetic resonance experiments were performed on a Bruker Elexys E580 operating at ~9.6 GHz and 0.34 T. Modulation was 100 kHz and modulation amplitude was kept in the range 0.02–0.05 mT, which is below the radical linewidth. The EPR spectra were fitted with the Matlab package Easyspin.[58,59] Other characterizations and the calibration experiments in Fig. 2c were performed on a Bruker ECS106 spectrometer operating at 9.6 GHz (see SI for details).

Dynamic nuclear polarization: experiments

DNP measurements at 1.2 T were performed on a Bruker Elexys E580 operating at 34 GHz with 40 W microwave (MW) power interfaced with a Bruker Avance III console for NMR detection.[26] The double resonance (electron and ^{13}C) probe consists of a cavity for MW irradiation, and a custom-made copper coil for radiofrequency irradiation and detection.[26] In the case of ^{13}C, the excitation and detection are at ~13 MHz. Samples were ~7 μL in volume sealed in a 1.6 mm outer diameter quartz tube. The lack of active cooling in combination with the small sample volume prevented the use of neat ^{13}C-MeOH due to its high MW absorption.

The DNP instrument at 9.4 T consists of a 263 GHz gyrotron, an NMR magnet, and a ^{1}H–^{13}C double-resonance probe with MW irradiation specifically designed for experiments in liquids.[27] Samples were prepared by degassing *via* freeze–pump–thaw cycles ~60–70 μL of sample and transferring it in a 5 mm outer-diameter quartz tube. A 4 mm outer diameter tube was used as an insert to decrease the sample thickness along the MW propagation direction, which is orthogonal to the tube axis.[27] The temperature of the sample under MW irradiation was controlled with a flow of cold nitrogen gas. Despite the sample being exposed to high-power MW irradiation, we did not notice any degradation of the AuNPs, which could arise if the temperature of the sample is not optimally controlled.

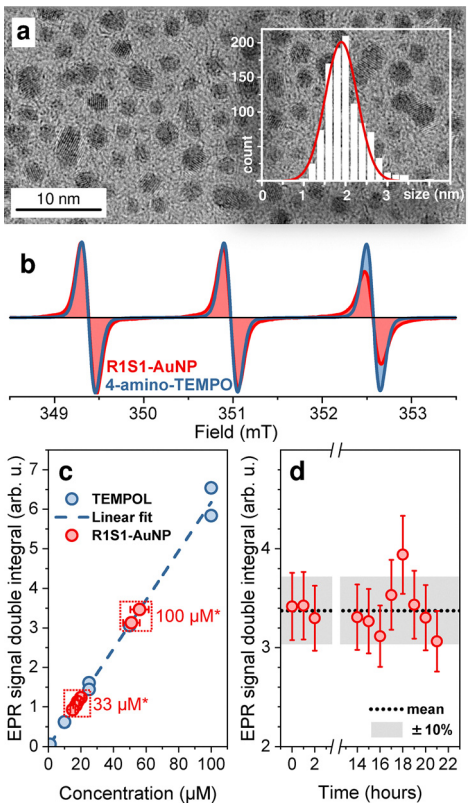

Fig. 2 (a) TEM image of the sample **R1S1-AuNP**, and histogram of the gold core size distribution. The curve was fitted with a Gaussian distribution with mean and standard deviation d_{Au} = 1.90 ± 0.38 nm. (b) CW-EPR spectra of 4-Amino-TEMPO and **R1S1-AuNP** in solutions recorded at 9 GHz. The intensities have been normalized. The area under the peaks (highlighted in color) is calculated by taking the double-integral of the spectrum. (c) Calibration curve for the radical concentration obtained for 4-amino-TEMPO (blue) and calibrated data for sample **R1S1-AuNP**. The numbers marked with * indicate the nominal concentration of **R1** estimated from structural data. (d) Double-integral value of CW-EPR spectra recorded over ~24 hours on a sample of **R1S1-AuNP** dispersed in $CHCl_3$. The grey bands indicate ±10% around the mean value (dotted line).

Dynamic nuclear polarization: theory

The spin polarization transfer between electron and nuclei is driven by the modulation of the electron–nuclear hyperfine couplings, both scalar and dipolar, which give counteractive contributions. Molecular mobility, and in particular the relative motions between the PA and the target molecule, determines the ratio of the two: molecular diffusion (translation and rotation) modulates the dipolar coupling, while molecular collisions modulate the scalar one. The NMR enhancements ε is given by the Overhauser equation:

$$\varepsilon = 1 - s \cdot f \cdot \xi \cdot \frac{|\gamma_e|}{\gamma_{13C}} \quad (1)$$

where: $|\gamma_e|$ and γ_{13C} are the electronic and nuclear gyromagnetic ratio, respectively; s is the saturation factor, namely the degree of saturation of the electron resonance; f (leakage factor) is the contribution of the paramagnetic relaxation over the total nuclear relaxation; and ξ is the coupling factor, which defines the efficiency of the spin polarization transfer process.

When experiments are performed under similar conditions (microwave irradiation, sample formulation) the DNP efficiency, and therefore the enhancement, depends mainly on how the molecular motions modulate the electron nuclear hyperfine coupling, *i.e.* on ξ. The coupling factor ξ can be written as a function of the spectral densities $J(\omega)$ associated with given molecular motions:

$$\xi = \frac{5}{7}\cdot\left(1-\frac{7k_D J_D(\omega_n,\tau_D)+7k_{rot}J_{rot}(\omega_n,\tau_{rot})}{R_1}\right)+ -\frac{12}{5}\cdot\left(\frac{0.5J_{sc}(\omega_e,\tau_{sc})}{R_1}\right), \quad (2)$$

where ω_n and ω_e are the nuclear and electron Larmor frequencies, respectively; τ_i are the correlation times; k_i are constants. The subscript "D" indicates the terms describing the translational diffusion, "rot" the rotational diffusion, and "sc" the scalar coupling. The term R_1 is the sum of all contributions:

$$R_1 = \frac{1}{2}J_{sc}(\omega_e,\tau_{sc}) + \sum_{i=D,rot} k_i[7J_i(\omega_e,\tau_i)+3J_i(\omega_e,\tau_i)]. \quad (3)$$

Results and discussion

Structural characterization

The size and size-distribution of **R1SX-AuNP**s was estimated by transmission electron microscopy (TEM) images taken after the synthesis (Fig. 2a and SI). The average size of the gold core is $d_{Au} \lesssim 1.9$ nm, while the size distribution follows a narrow Gaussian profile (Fig. 2a and Table 1). UV-vis spectra validate these results and confirm that the average size of the gold core is $d_{Au} < 2$ nm (SI).

With the morphological data obtained from TEM and thermogravimetric analysis (TGA), and considering the amount of radical thiol **S1** added in the synthesis step (SI), we estimated the average composition of **R1SX-AuNP**s. However, to precisely estimate the amount of radical thiol **R1** grafted on the Au-NPs surface, we utilized CW-EPR (Fig. 2b). Specifically, we quantified the number of unpaired electron spins in the sample, which is proportional to the double integral of the EPR spectrum (Fig. 2b). A calibration curve was obtained by dissolving 4-Amino-TEMPO in dichloromethane with precise concentrations ranging from 1 μM to 100 μM (Fig. 2b). Using this same procedure and ensuring consistency in solvent, sample tubes, and sample volume, we prepared samples of **R1SX-AuNP** with known concentration of radical thiol **R1** derived from the structural characterization obtained with TEM and TGA (Fig. 2a and Fig. S15). From this analysis we estimated that the amount of radical thiol **R1** over the total amount of thiols grafted onto the gold surface is ∼5% for **R1S1-AuNP**, and ∼7.5% for **R1S2-AuNP** (Table 1). Notably, AuNPs without **R1** functionalization do not show any EPR signal.

To verify the stability of **R1SX-AuNP**s in organic solvents, we conducted spin counting experiments with CW-EPR as a function of time. As representative sample, we selected **R1S1-AuNP** dissolved in $CHCl_3$ and monitored it over approximately 24 hours. The results (Fig. 2c) show that the double-integral values fluctuate by ∼10% around the mean value, possibly due to slightly different experimental conditions (temperature and sample positioning in the resonator), but there is no indication of radical quenching. Importantly, the shape of the CW-EPR spectrum does not change over time, indicating that the radical thiol **R1** does not detach from the AuNPs.

Radical mobility *via* EPR

The CW-EPR spectrum of a nitroxide radical dispersed in low-viscosity organic solvents (*e.g.* $CHCl_3$, CH_2Cl_2) shows three lines separated by the isotropic hyperfine coupling A_{iso}, which are equally intense due to the complete averaging of the g-tensor due to the fast tumbling of the molecule (Fig. 2b). This is also the case for radical thiol **2** (Fig. 3a). When the mobility of the radical is constrained, as in the case of **R1** bound to AuNPs, the g-tensor is only partially averaged. This causes the lines to broaden, and the high-field line to appear less intense (Fig. 3b and c). Considering the difference in EPR spectra between radicals bound to the AuNPs and those that remain unbound, the spectra of samples **R1S1-AuNP** and **R1S2-AuNP** (Fig. 3b and c) indicate that all radicals are bound to the AuNPs, as there is no contribution from fast-tumbling nitroxides that might have remained unbound during the synthesis. This is further corroborated by the fact that the spectra can be fitted with a single component.

The rotational correlation time τ_c was estimated by fitting the CW EPR spectra. Nitroxide radicals TEMPOL and TEMPONE as well as radical thiol **2** have correlation times of few picoseconds (∼7 ps and ∼5 ps, respectively, Table 2). When the radical thiol is grafted onto the AuNP surface (**R1**), its mobility is drastically reduced, as evidenced by the reduced intensity and broadening of the high field line in the CW-EPR

Table 1 Structural properties of AuNPs systems. The diameter of the gold core d_{Au} was obtained by TEM measurements, and the values indicate the mean of the Gaussian distribution of sizes and its standard deviation. The thiols surface density and the total number of thiols per single AuNP were obtained by TEM and TGA (Supplementary Information), while the amount of radical thiol **R1** was quantified with CW-EPR

Sample	Synthesis method	Formula	d_{Au} (nm)	Thiols surface density (nm^{-2})	Total thiols per AuNP	**R1**/total thiols
R1S1-AuNP	Chemical exchange	$Au_{211}R1_{17}S1_{125}$	1.90 ± 0.38	11.6	132	5.3 ± 0.3%
R1S2-AuNP	Direct synthesis	$Au_{134}R1_5S2_{67}$	1.63 ± 0.30	8.6	72	7.5 ± 0.7%

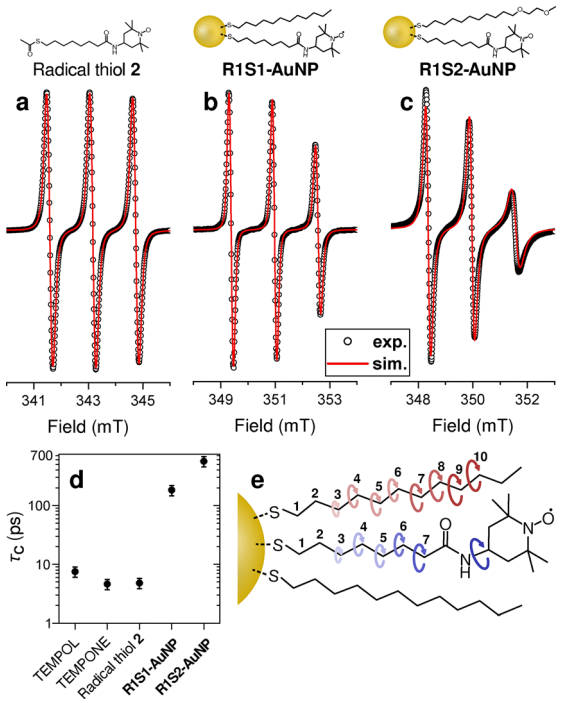

Fig. 3 CW-EPR spectra and fit. (a)–(e) CW EPR spectra recorded at 9 GHz for TM-thiol **2**, **R1S1-AuNP**, and **R1S2-AuNP**. Fits (solid lines) are obtained with the Matlab package *Easyspin* using the fitting routine for slow motions regimes (*chili*). Magnetic field axis are not calibrated. (d) Correlation times obtained from the fit of EPR spectra. Error bars are estimated by averaging the result from multiple samples. (e) Sketch of the mobility of thiols. Red arrows indicate the mobility of the methyl groups on the alkyl chain **S1** as assessed by Piserchia *et al.*, 2015.[63] We infer that the same mobility is retained for the alkyl chain of TM-thiol **2** (blue arrows). The amine group has free rotational freedom along the bond axis.

spectra (Fig. 3b and c). In particular, the longer the chain of the thiol adjacent to **R1**, the slower the correlation time, which increases from τ_c = 183 ps for **R1S1-AuNP** to τ_c = 565 ps for **R1S2-AuNP** (Fig. 3d and Table 2).

These correlation times are comparable to those reported for fullerenes (C_{60}) functionalized with nitroxide derivatives, which have also been used as PAs for OE-DNP.[33] In our case, the correlation time τ_c of the radical thiol **R1** is shorter than the correlation time of the whole AuNP system, $\tau_{c,NP}$. The latter can be qualitatively assessed with the Stokes–Einstein–Debye equation $\tau_{c,NP} = 4\pi\cdot\eta\cdot r^3/(3\cdot k_B T)$,[60,61] where η = 0.563 mPa s is the viscosity of $CHCl_3$ at room temperature, r is the radius of the object, and $k_B T$ is the thermal energy. Considering the radius of the gold core ($r_{Au} = d_{Au}/2$) and the length of the thiol chain fully extended, the resulting correlation time is at most τ_c = 4.6 ns, an upper bound estimate within the limits of the current model (Table 2). As demonstrated in a previous study, the mobility of the carbons in the alkyl chain increases upon moving away from the AuNP surface (Fig. 3e). Therefore, the radical thiol **R1** retains a degree of mobility due to flexibility, even when grafted on the NP surface (Fig. 3e). It is worth pointing out that, in the case of TEMPO radicals grafted on a silica surfaces, the solutions are heterogeneous and exhibit a much-reduced mobility of the radical moiety.[47]

Table 2 Correlation times τ_c of the radical are obtained from fitting the CW-EPR spectra. Fits were performed with *Easyspin*, using the routine chili. Error bars (in parentheses) are estimated from fitting multiple spectra. The correlation time of the AuNP $\tau_{c,NP}$ has been estimated with the Stokes–Eistein–Debye equation with the radius r_{Au} given by $r_{Au} = d_{Au}/2 + l_{SX}$ where l_{SX} were estimated considering the chain fully extended and are l_{S1} = 1.4 nm and l_{S2} = 1.7 nm. The viscosity of $CHCl_3$ is η = 0.563 mPa s at 20 °C

Radical	τ_c (ps)	$\tau_{c,NP}$ (ps)
TEMPOL	7(1)	—
TEMPONE	5(1)	—
TM thiol 2	5(1)	—
R1S1-AuNP	183(33)	3.7×10^3
R1S2-AuNP	565(113)	4.6×10^3

Nanoparticle-assisted dynamic nuclear polarization

The recognition capabilities of **R1S2-AuNP** were tested by ^{1}H-NMR. To avoid the effect of paramagnetic broadening of the NMR lines caused by the TEMPO headgroup, we tested AuNPs bearing only the group **S2** (**S2-AuNP**). The AuNPs were dissolved in CD_2Cl_2 along with $CHCl_3$ and MeOH, both at 20 mM. Fig. 4 shows a comparison of this spectrum with that obtained from a similar system without nanoparticles. There is a marked broadening of the MeOH signals in the presence of **S2-AuNPs** (Fig. 4c), whereas the signals of $CHCl_3$ are unaffected (Fig. 4b). This effect likely arises from the tendency of **S2-AuNPs** to act as hydrogen bond acceptors for MeOH molecules, thus concentrating them in the monolayer and increasing the exchange rate of OH protons. It is it worth pointing out that such evidence could not be corroborated by saturation transfer experiments typically used in NMR chemosensing, due to the overlap between the MeOH signals and those arising from the oxomethylene headgroups of **S2** (~3.5 ppm in Fig. 4).

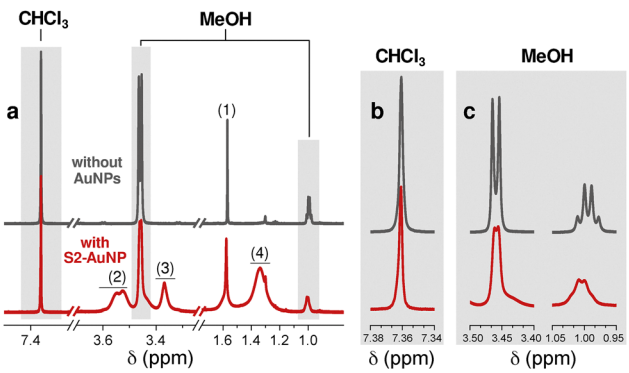

Fig. 4 500 MHz ^{1}H NMR. (a) NMR spectra of $CHCl_3$ 20 mM + MeOH 20 mM in CD_2Cl_2 recorded at 298 K without (black) and with (red) additional 5 mM **S2-AuNP**, without the TEMPO headgroup. Other peaks are assigned to residual H_2O (1) and to the thiols of **S2-AuNP**: (2) OCH_2CH_2; (3) OCH_3; (4) OCH_2. (b) Magnification of the line of $CHCl_3$, which is virtually unaffected by the presence of AuNPs. (c) Magnification of the peaks of MeOH, which appear broadened due to fast chemical exchange with **S2-AuNP**.

Nonetheless, as a control experiment, we acquired ^{1}H NMR spectra at varying temperatures (298 K, 283 K, and 278 K). These spectra exhibit changes predominantly limited to the chemical shifts of the peaks (see SI), thereby suggesting that the line broadening observed in presence of **S1**-AuNPs is unlikely due to be due to a decrease in correlation time but rather due to chemical exchange.

We performed OE-DNP experiments both at low (1.2 T) and high magnetic fields (9.4 T) recording the ^{13}C enhancements ($^{13C}\varepsilon$) on $CHCl_3$ and on mixtures of $CHCl_3$ and MeOH doped with **R1SX-AuNP**s or nitroxide radicals. The results are summarized in Fig. 5. At 1.2 T, $^{13C}\varepsilon$ on $CHCl_3$ doped with **R1S1-AuNP** is $^{13C}\varepsilon \sim 145$, which is only ~25% smaller than $^{13C}\varepsilon = 195$ obtained with TEMPOL (Fig. 5a). At 9.4 T, we tested a mixture of 500 mM ^{13}C-$CHCl_3$ and 500 mM of ^{13}C-MeOH dispersed in $CHCl_3$. The analyte concentration was selected as in ref. 27 in order to optimize the ^{13}C sensitivity and the acquisition time on the DNP instrument. Once again, the enhancements obtained with TEMPOL ($^{13C}\varepsilon \sim 60$ on ^{13}C-$CHCl_3$ and $^{13C}\varepsilon \sim 5$ on ^{13}C-MeOH) are larger than those obtained with **R1SX-AuNP**: on $CHCl_3$, **R1S1-AuNPs** provide $^{13C}\varepsilon \sim 24$, which is further reduced to $^{13C}\varepsilon \sim 5$ when using **R1S2-AuNPs** (Fig. 5b). Although **R1S2-AuNPs** recognize MeOH molecules, we do not observe an enhancement on ^{13}C-MeOH.

These results can be interpreted with analytical models that describe the spin dynamics of OE-DNP in the liquid state (eqn 2).[19,25,33,34,62] All $^{13C}\varepsilon$ measured on ^{13}C-$CHCl_3$ are positive, indicating that the electron–nuclear scalar coupling is larger than the competing dipolar one.[35] The rotational correlation time of the radical can contribute to the electron–nuclear dipolar coupling when for $\tau_c > 10$–20 ps, effectively counteracting the scalar coupling and therefore reducing the enhancements.[33,62]

Using the approach discussed in ref. 33, eqn (1) and (2) with $\tau_{rot} = \tau_c$, we extrapolated the $^{13C}\varepsilon$ enhancements as a function of the rotational correlation time τ_c of the radical (Fig. 5c), which is included in the term $J_{rot}(\omega,\tau_c)$ in eqn (2), while considering unchanged all the other elements in the equations (s and f in eqn (1), $J_D(\omega,\tau_D)$ and $J_{sc}(\omega,\tau_{sc})$) in eqn (2). Despite the crude approximation, the simulations reproduce the trend observed in the experimental data and suggest that the low $^{13C}\varepsilon$ observed for **R1SX-AuNP** can be mainly ascribed to the slow rotation of the radical. By way of comparison, nitroxides grafted on silica surfaces show τ_c of the radical on the order of few nanoseconds,[47] which would lead to lower DNP performances at high magnetic fields as compared to AuNPs.

Finally, we will discuss why MeOH is not an optimal target for NP mediated OE-DNP, despite **R2S2-AuNPs** effectively working as molecular recognition agents for it. As suggested by our simulations on ^{13}C-$CHCl_3$ data, the enhancement $^{13C}\varepsilon \sim 5$ obtained with TEMPOL should be reduced by ≥60% in presence of **R1S2-AuNPs** solely due to the radical mobility making it undetectable under our experimental conditions. Second, the requirements for an optimal agent for chemosensing and an optimal PA for OE-DNP are different. The spin polarization transfer in OE-DNP is very effective when there are modulations of the electron–nuclear hyperfine coupling on the order of the electron Larmor frequency ($J(\omega_e)$, eqn (2)): these arise from fast molecular dynamics (collisions, vibrations) on the order of picoseconds and lower. In contrast, as far as NMR chemosensing is concerned, effective nuclear-nuclear cross-relaxation requires the analyte's residence time within the monolayer to be comparable to, or exceed, the nanoparticle's rotational correlation time ($\tau_{c,NP}$), which is in the order of nanoseconds. This discrepancy in the dynamics might explain the limited efficacy of **R1SX-AuNP**s in polarizing the recognized target molecule *via* OE-DNP.

To possibly overcome these limitations and effectively enable molecular recognition, it appears necessary to modify the organic thiol and/or the linker to the nitroxide to adjust the mobility. AuNPs are an ideal platform for this task, due to the versatile chemistry of their monolayers, which can be controlled by adjusting the length and nature of the spacer between the Au core and

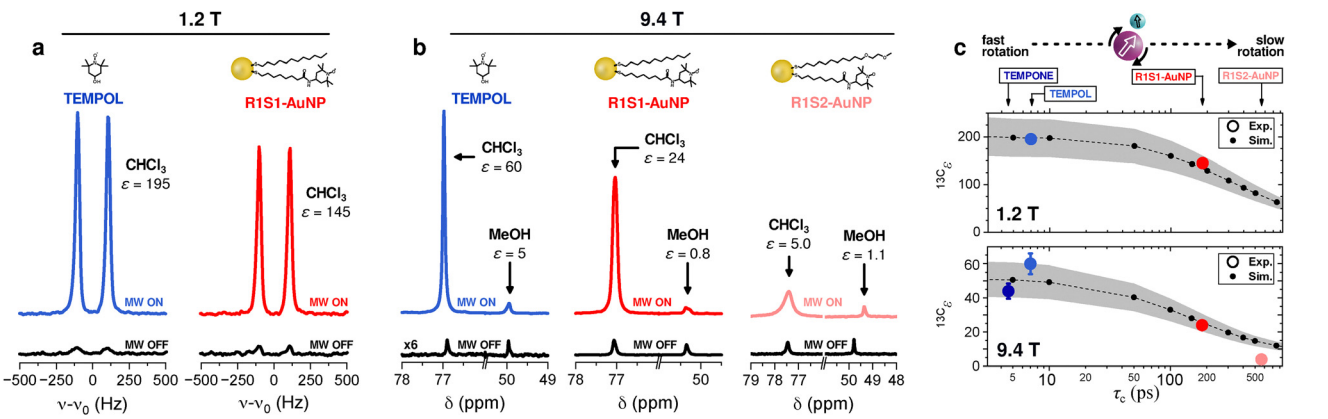

Fig. 5 (a) MW on and MW off ^{13}C DNP-NMR spectra of $CHCl_3$ doped with TEMPOL and **R1S1-AuNPs**. Spectra were rescaled to the same noise level. (b) MW on and MW off ^{13}C DNP-NMR spectra of ^{13}C-$CHCl_3$ (500 mM) and ^{13}C-MeOH (500 mM) dissolved in $CHCl_3$ and doped with (c) TEMPOL, and **R1S1-AuNPs**, and **R1S2-AuNPs**. Spectra were acquired with ^{1}H decoupling. The vertical axis is in arbitrary. (c) Experimental and predicted ^{13}C-NMR enhancements of ^{13}C-$CHCl_3$ as a function of the PA correlation time. $^{13C}\varepsilon$ at 1.2 T and 9.4 T plotted as a function of the rotational correlation time τ_c estimated from the EPR measurements. units. The colored band represents an error bar of 20% on the simulated points.

the headgroup, as well as by leveraging inter-chain interactions. Alongside this "direct" approach, where the nanoparticle headgroup carries the unpaired electron, we are currently investigating the feasibility of a "reverse" approach, wherein the nanoparticle headgroup is functionalized with a suitable moiety to be polarized through interaction with a radical species present in solution.

Conclusions

In this study, we investigated the feasibility of achieving selective OE-DNP in the liquid state by designing monolayer-protected nanoparticles that combine molecular recognition properties with the ability to function as polarizing agents for OE-DNP. Specifically, we designed and synthesized AuNPs (<2 nm in diameter) functionalized both with nitroxide radicals to act as PAs and with organic thiols that favour the formation of hydrogen bond networks. The morphological characterization shows that functionalized AuNPs are soluble and stable in organic solvents, and that the radical headgroup retains fast mobility (correlation time $\tau_c \sim 200$–600 ps) thanks to the flexibility of the alkyl chain. Furthermore, AuNPs act as a molecular recognition agents for MeOH, as demonstrated by the increased line broadening due to its interaction with the monolayer. With OE-DNP measurements performed at low (1.2 T) and high (9.4 T) magnetic fields, we showed that AuNPs can be used as PAs. Although the interaction between MeOH and the functionalized AuNPs does not lead to a significantly enhanced polarization efficiency—likely due to the restrained mobility of the nitroxide headgroup—our results validate these nanostructures as viable polarizing agents in the context of OE-DNP. Furthermore, under optimal conditions, they might enable DNP-enhanced NMR-chemosensing experiments in solution for targeted selective DNP of small molecules. While silica has been suggested as a substrate to graft PAs, the modular and tunable surface chemistry of AuNPs establishes them as an ideal platform for designing DNP systems with additional chemosensing capabilities in solution. By exploiting diverse interactions, including hydrophobic forces, ion pairing, and metal–ligand coordination, these nanoreceptors can be precisely engineered to provide highly specific binding sites across a broad range of substrates. Indeed, the extensive variety of monolayers that can be assembled enables fine-tuning not only toward analyte selectivity but also over the strength and potentially over the dynamic features of the analyte binding process. Together, these features make AuNPs a uniquely controllable platform for precise modulation of analyte binding thermodynamics and kinetics, enabling the development of highly versatile chemosensors.

Author contributions

FR, FM, and TO conceived the study; BBM and GZ synthesized and characterized the compounds; BBM, LF, and TO performed EPR measurements and analysis; LY, AvdH, and TO performed the DNP measurements; BBM and FR performed the NMR measurements; TO and FR analysed the data. FR and TO wrote the original draft and the final version was approved by all the authors.

Conflicts of interest

There are no conflicts to declare.

Data availability

The data supporting this article have been included as part of the SI: Synthesis of and functionalization of AuNPs, morphological characterization, NMR and EPR characterization, DNP results. See DOI: **https://doi.org/10.1039/d5cp02465j**

Acknowledgements

TO acknowledges the support of FSU-SEED grant awarded by Florida State University, and the grant number 455993474 (2021-2022) awarded by the German Research Foundation (DFG). Part of this work was performed at the National High Magnetic Field Laboratory (NHMFL), which is supported by the National Science Foundation (NSF) through NSF/DMR-2128556 and the State of Florida. Part of this work was funded by the Italian Association for Cancer Research (AIRC) under the Investigators Grants scheme (IG 25003), and by the NSF/CHE-2320338. BM acknowledges the support of the GIDRM Mobility Grant 2024. The authors acknowledge Marina Bennati and Stephen Hill for helpful discussions and access to DNP instruments.

Notes and references

1 N. A. Kotov, Inorganic Nanoparticles as Protein Mimics, *Science*, 2010, **330**, 188–189.
2 A. Quarta, A. Curcio, H. Kakwere and T. Pellegrino, Polymer coated inorganic nanoparticles: tailoring the nanocrystal surface for designing nanoprobes with biological implications, *Nanoscale*, 2012, **4**, 3319–3334.
3 L. Riccardi, L. Gabrielli, X. Sun, F. De Biasi, F. Rastrelli, F. Mancin and M. De Vivo, Nanoparticle-Based Receptors Mimic Protein-Ligand Recognition, *Chem*, 2017, **3**, 92–109.
4 U. Drechsler, B. Erdogan and V. M. Rotello, Nanoparticles: Scaffolds for Molecular Recognition, *Chem. – Eur. J.*, 2004, **10**, 5570–5579.
5 E. C. Dreaden, A. M. Alkilany, X. Huang, C. J. Murphy and M. A. El-Sayed, The golden age: gold nanoparticles for biomedicine, *Chem. Soc. Rev.*, 2012, **41**, 2740–2779.
6 K. Saha, S. S. Agasti, C. Kim, X. Li and V. M. Rotello, Gold nanoparticles in chemical and biological sensing, *Chem. Rev.*, 2012, **112**, 2739–2779.
7 M. Boccalon, P. Franchi, M. Lucarini, J. J. Delgado, F. Sousa, F. Stellacci, I. Zucca, A. Scotti, R. Spreafico, P. Pengo and L. Pasquato, Gold nanoparticles protected by fluorinated ligands for 19F MRI, *Chem. Commun.*, 2013, **49**, 8794–8796.

8 L. Gabrielli, L. J. Prins, F. Rastrelli, F. Mancin and P. Scrimin, Hydrolytic Nanozymes, *Eur. J. Org. Chem.*, 2020, 5044–5055.
9 F. De Biasi, F. Mancin and F. Rastrelli, Nanoparticle-assisted NMR spectroscopy: A chemosensing perspective, *Prog. Nucl. Magn. Reson. Spectrosc.*, 2020, **117**, 70–88.
10 I. de Lázaro and D. J. Mooney, Obstacles and opportunities in a forward vision for cancer nanomedicine, *Nat. Mater.*, 2021, **20**, 1469–1479.
11 B. Perrone, S. Springhetti, F. Ramadori, F. Rastrelli and F. Mancin, "NMR chemosensing" using monolayer-protected nanoparticles as receptors, *J. Am. Chem. Soc.*, 2013, **135**, 11768–11771.
12 F. De Biasi, B. B. Mascitti, E. Kupče and F. Rastrelli, Uniform water-mediated saturation transfer: A sensitivity-improved alternative to WaterLOGSY, *J. Magn. Reson.*, 2022, **338**, 107190.
13 J. Eills, D. Budker, S. Cavagnero, E. Y. Chekmenev, S. J. Elliott, S. Jannin, A. Lesage, J. Matysik, T. Meersmann, T. Prisner, J. A. Reimer, H. Yang and I. V. Koptyug, Spin Hyperpolarization in Modern Magnetic Resonance, *Chem. Rev.*, 2023, **123**, 1417–1551.
14 N. K. J. Hermkens, N. Eshuis, B. J. A. van Weerdenburg, M. C. Feiters, F. P. J. T. Rutjes, S. S. Wijmenga and M. Tessari, NMR-Based Chemosensing *via* p-H_2 Hyperpolarization: Application to Natural Extracts, *Anal. Chem.*, 2016, **88**, 3406–3412.
15 R. Fraser, F. P. J. T. Rutjes, M. C. Feiters and M. Tessari, Analysis of Complex Mixtures by Chemosensing NMR Using para-Hydrogen-Induced Hyperpolarization, *Acc. Chem. Res.*, 2022, **55**, 1832–1844.
16 A. W. Overhauser, Polarization of nuclei in metals, *Phys. Rev.*, 1953, **92**, 411–415.
17 K. H. Hausser and D. Stehlik, in *Advances in Magnetic Resonance*, ed J. S. Waugh, Academic Press, 1968, vol. 3, pp. 79–139.
18 M. Bennati, I. Tkach and M. T. Türke, Dynamic nuclear polarization in liquids, *Electron Paramagn. Reson.*, 2011, **22**, 155–182.
19 E. Ravera, C. Luchinat and G. Parigi, Basic facts and perspectives of Overhauser DNP NMR, *J. Magn. Reson.*, 2016, **264**, 78–87.
20 M. Bennati and T. Orlando, Overhauser DNP in liquids on ^{13}C nuclei, *eMagRes*, 2019, **8**, 11–18.
21 X. Wang, W. C. Isley III, S. I. Salido, Z. Sun, L. Song, K. H. Tsai, C. J. Cramer and H. C. Dorn, Optimization and prediction of the electron–nuclear dipolar and scalar interaction in ^{1}H and ^{13}C liquid state dynamic nuclear polarization, *Chem. Sci.*, 2015, **6**, 6482–6495.
22 S. E. Küçük and D. Sezer, Multiscale computational modeling of ^{13}C DNP in liquids, *Phys. Chem. Chem. Phys.*, 2016, **18**, 9353–9357.
23 V. P. Denysenkov and T. F. Prisner, Liquid-state Overhauser DNP at High Magnetic Fields, *eMagRes*, 2019, **8**, 41–54.
24 J. L. Russ, J. Gu, K. H. Tsai, T. Glass, J. C. Duchamp and H. C. Dorn, Nitroxide/substrate weak hydrogen bonding: Attitude and dynamics of collisions in solution, *J. Am. Chem. Soc.*, 2007, **129**, 7018–7027.
25 T. Orlando, I. Kuprov and M. Hiller, Theoretical analysis of scalar relaxation in ^{13}C-DNP in liquids, *J. Magn. Reson. Open*, 2022, **10–11**, 100040.
26 T. Orlando, R. Dervişoğlu, M. Levien, I. Tkach, T. F. Prisner, L. B. Andreas, V. P. Denysenkov and M. Bennati, Dynamic Nuclear Polarization of 13C Nuclei in the Liquid State over a 10 Tesla Field Range, *Angew. Chem., Int. Ed.*, 2019, **58**, 1402–1406.
27 M. Levien, L. Yang, A. van der Ham, M. Reinhard, M. John, A. Purea, J. Ganz, T. Marquardsen, I. Tkach, T. Orlando and M. Bennati, Overhauser enhanced liquid state nuclear magnetic resonance spectroscopy in one and two dimensions, *Nat. Commun.*, 2024, **15**, 5904.
28 L. Yang, T. Orlando and M. Bennati, Halogen-Bond-Mediated ^{13}C Overhauser Dynamic Nuclear Polarization at 9.4 T, *J. Phys. Chem. Lett.*, 2025, 4505–4514.
29 M. Reinhard, M. Levien, M. Bennati and T. Orlando, Large ^{31}P-NMR enhancements in liquid state dynamic nuclear polarization through radical/target molecule non-covalent interaction, *Phys. Chem. Chem. Phys.*, 2023, **25**, 822–828.
30 W. Müller-Warmuth, R. Vilhjalmsson, P. A. M. Gerlof, J. Smidt and J. Trommel, Intermolecular interactions of benzene and carbon tetrachloride with selected free radicals in solution as studied by ^{13}C and ^{1}H dynamic nuclear polarization, *Mol. Phys.*, 1976, **31**, 1055–1067.
31 S. G. J. Van Meerten, M. C. D. Tayler, A. P. M. Kentgens and P. J. M. van Bentum, Towards Overhauser DNP in supercritical CO2, *J. Magn. Reson.*, 2016, **267**, 30–36.
32 D. Sezer, Rationalizing Overhauser DNP of nitroxide radicals in water through MD simulations, *Phys. Chem. Chem. Phys.*, 2014, **16**, 1022–1032.
33 M. Levien, M. Hiller, I. Tkach, M. Bennati and T. Orlando, Nitroxide Derivatives for Dynamic Nuclear Polarization in Liquids: The Role of Rotational Diffusion, *J. Phys. Chem. Lett.*, 2020, **11**, 1629–1635.
34 M. Bennati, C. Luchinat, G. Parigi and M. T. Türke, Water ^{1}H relaxation dispersion analysis on a nitroxide radical provides information on the maximal signal enhancement in Overhauser dynamic nuclear polarization experiments, *Phys. Chem. Chem. Phys.*, 2010, **12**, 5902–5910.
35 G. Parigi, E. Ravera, M. Bennati and C. Luchinat, Understanding Overhauser Dynamic Nuclear Polarisation through NMR relaxometry, *Mol. Phys.*, 2019, **117**, 888–897.
36 P. Neugebauer, J. G. Krummenacker, V. P. Denysenkov, C. Helmling, C. Luchinat, G. Parigi and T. F. Prisner, High-field liquid state NMR hyperpolarization: a combined DNP/NMRD approach, *Phys. Chem. Chem. Phys.*, 2014, **16**, 18781–18787.
37 S. E. Küçük, P. Neugebauer, T. F. Prisner and D. Sezer, Molecular simulations for dynamic nuclear polarization in liquids: A case study of TEMPOL in acetone and DMSO, *Phys. Chem. Chem. Phys.*, 2015, **17**, 6618–6628.

38 J. Van Bentum, B. Van Meerten, M. Sharma and A. P. M. Kentgens, Perspectives on DNP-enhanced NMR spectroscopy in solutions, *J. Magn. Reson.*, 2016, **264**, 59–67.
39 G. Liu, M. Levien, N. Karschin, G. Parigi, C. Luchinat and M. Bennati, One-thousand-fold enhancement of high field liquid nuclear magnetic resonance signals at room temperature, *Nat. Chem.*, 2017, **9**, 676–680.
40 O. Jakdetchai, V. P. Denysenkov, J. Becker-Baldus, B. Dutagaci, T. F. Prisner and C. Glaubitz, Dynamic nuclear polarization-enhanced NMR on aligned lipid bilayers at ambient temperature, *J. Am. Chem. Soc.*, 2014, **136**, 15533–15536.
41 A. A. Kuzhelev, D. Dai, V. P. Denysenkov and T. F. Prisner, Solid-like Dynamic Nuclear Polarization Observed in the Fluid Phase of Lipid Bilayers at 9.4 T, *J. Am. Chem. Soc.*, 2022, **144**, 1164–1168.
42 A. A. Kuzhelev, V. Denysenkov, I. M. Ahmad, O. Yu. Rogozhnikova, D. V. Trukhin, E. G. Bagryanskaya, V. M. Tormyshev, S. Th. Sigurdsson and T. F. Prisner, Solid-Effect Dynamic Nuclear Polarization in Viscous Liquids at 9.4 T Using Narrow-Line Polarizing Agents, *J. Am. Chem. Soc.*, 2023, **145**, 10268–10274.
43 Y. Rao, D. Gioffrè, M. Levien, M. Wörle, P. Pandey, M. Mazzanti, C. Copéret and L. Emsley, Surface Enhanced Nuclear Magnetic Resonance Spectroscopy at Solid–Liquid Interfaces Using Overhauser Dynamic Nuclear Polarization, *J. Am. Chem. Soc.*, 2025, **147**(25), 21297–21301.
44 N. M. Loening, M. Rosay, V. Weis and R. G. Griffin, Solution-state dynamic nuclear polarization at high magnetic field, *J. Am. Chem. Soc.*, 2002, **124**, 8808–8809.
45 Y. Rao, F. De Biasi, R. Wei, C. Copéret and L. Emsley, Probing Homogeneous Catalysts and Precatalysts in Solution by Exchange-Mediated Overhauser Dynamic Nuclear Polarization NMR, *J. Am. Chem. Soc.*, 2024, **146**(18), 12587–12594.
46 R. Gitti, C. Wild, C. Tsiao, K. Zimmer, T. E. Glass and H. C. Dorn, Solid-Liquid Intermolecular Transfer of Dynamic Nuclear Polarization. Enhanced Flowing Fluid ^{1}H NMR Signals *via* Immobilized Spin Labels, *J. Am. Chem. Soc.*, 1988, **110**, 2294–2296.
47 H. C. Dorn, T. E. Glass, R. Gitti and K. H. Tsai, Transfer of ^{1}H and ^{13}C dynamic nuclear polarization from immobilized nitroxide radicals to flowing liquids, *Appl. Magn. Reson.*, 1991, **2**, 9–27.
48 N. Enkin, G. Liu, M. del, C. Gimenez-Lopez, K. Porfyrakis, I. Tkach and M. Bennati, A high saturation factor in Overhauser DNP with nitroxide derivatives: the role of ^{14}N nuclear spin relaxation, *Phys. Chem. Chem. Phys.*, 2015, **17**, 11144–11149.
49 T. V. Can, M. A. Caporini, F. Mentink-Vigier, B. Corzilius, J. J. Walish, M. Rosay, W. E. Maas, M. Baldus, S. Vega, T. M. Swager and R. G. Griffin, Overhauser effects in insulating solids, *J. Chem. Phys.*, 2014, **141**, 064202.
50 Y. Li, A. Equbal, T. Tabassum and S. Han, ^{1}H Thermal Mixing Dynamic Nuclear Polarization with BDPA as Polarizing Agents, *J. Phys. Chem. Lett.*, 2020, **11**, 9195–9202.
51 F. A. Perras, F. Mentink-Vigier and S. Pylaeva, Perspectives on the Dynamic Nuclear Polarization Mechanisms of Monoradicals: Overhauser Effect or Thermal Mixing?, *J. Phys. Chem. Lett.*, 2025, **16**, 3420–3432.
52 R. Kircher, H. Hasse and K. Münnemann, High Flow-Rate Benchtop NMR Spectroscopy Enabled by Continuous Overhauser DNP, *Anal. Chem.*, 2021, **93**, 8897–8905.
53 S. Wi, A. Giannouli, K. Butbul, J. Lumata, T. Dubroca, F. Scott, Z. Dowdell, R. W. Schurko, H. Van Tol and L. Frydman, Toward Generalized Solution-State ^{1}H DNP NMR *via* Particle-Mediated Cross-Relaxation, *J. Phys. Chem. Lett.*, 2025, **16**, 6627–6636.
54 D. Gajan, M. Schwarzwälder, M. P. Conley, W. R. Grüning, A. J. Rossini, A. Zagdoun, M. Lelli, M. Yulikov, G. Jeschke, C. Sauvée, O. Ouari, P. Tordo, L. Veyre, A. Lesage, C. Thieuleux, L. Emsley and C. Copéret, Solid-phase polarization matrixes for dynamic nuclear polarization from homogeneously distributed radicals in mesostructured hybrid silica materials, *J. Am. Chem. Soc.*, 2013, **135**, 15459–15466.
55 A. M. Schrader, J. I. Monroe, R. Sheil, H. A. Dobbs, T. J. Keller, Y. Li, S. Jain, M. S. Shell, J. N. Israelachvili and S. Han, Surface chemical heterogeneity modulates silica surface hydration, *Proc. Natl. Acad. Sci. U. S. A.*, 2018, **115**, 2890–2895.
56 B. Gizatullin, C. Mattea and S. Stapf, Radicals on the silica surface: probes for studying dynamics by means of fast field cycling relaxometry and dynamic nuclear polarization, *Magn. Reson. Lett.*, 2023, **3**, 256–265.
57 V. Chechik, H. J. Wellsted, A. Korte, B. C. Gilbert, H. Caldararu, P. Ionita and A. Caragheorgheopol, Spin-labelled Au nanoparticles, *Faraday Discuss.*, 2004, **125**, 279–291.
58 S. Stoll and A. Schweiger, EasySpin, a comprehensive software package for spectral simulation and analysis in EPR, *J. Magn. Reson.*, 2006, **178**, 42–55.
59 S. Stoll and A. Schweiger, EasySpin: Simulating cw ESR spectra, *Biol. Magn. Reson.*, 2007, **27**, 299–321.
60 A. Einstein, On the movement of small particles suspended in stationary liquids required by the molecular-kinetic theory of heat, *Ann. Phys.*, 1905, **322**, 549–560.
61 N. L. Mandel, S. Lee, K. Kim, K. Paeng and L. J. Kaufman, Single molecule demonstration of Debye–Stokes–Einstein breakdown in polystyrene near the glass transition temperature, *Nat. Commun.*, 2022, **13**, 3580.
62 A. A. Kuzhelev, D. Dai, V. P. Denysenkov, I. A. Kirilyuk, E. G. Bagryanskaya and T. F. Prisner, Influence of Rotational Motion of Nitroxides on Overhauser Dynamic Nuclear Polarization: A Systematic Study at High Magnetic Fields, *J. Phys. Chem. C*, 2021, **125**, 25651–25659.
63 A. Piserchia, M. Zerbetto, M.-V. Salvia, G. Salassa, L. Gabrielli, F. Mancin, F. Rastrelli and D. Frezzato, Conformational Mobility in Monolayer-Protected Nanoparticles: From Torsional Free Energy Profiles to NMR Relaxation, *J. Phys. Chem. C*, 2015, **119**, 20100–20110.